Scatterer size estimation in pulse-echo ultrasound using focused sources: Theoretical approximations and simulation analysis

Timothy A. Bigelow and William D. O'Brien, Jr.[a)]
Bioacoustics Research Laboratory, Department of Electrical and Computer Engineering, University of Illinois, 405 North Mathews, Urbana, Illinois 61801

(Received 13 June 2003; revised 31 March 2004; accepted 12 April 2004)

The speckle in ultrasound images has long been thought to contain information related to the tissue microstructure. Many different investigators have analyzed the frequency characteristics of the backscattered signals to estimate the scatterer acoustic concentration and size. Previous work has been mostly restricted to unfocused or weakly focused ultrasound sources, thus limiting its implementation with diagnostically relevant fields. Herein, we derive equations capable of estimating the size of a scatterer for any reasonably focused source provided that the velocity potential field in the focal region can be approximated as a three-dimensional Gaussian beam, scatterers are a sufficient distance from the source, and the field is approximately constant across the scatterer. The calculations show that, when estimating the scatterer size, correcting for focusing requires a generalized attenuation-compensation function that includes both attenuation and focusing along the beam axis. The Gaussian approximation is validated by comparing the ideal velocity potential field for three spherically focused sources with *f*-numbers of 1, 2, and 4 to the Gaussian approximation for frequencies from 2 to 14 MHz. The theoretical derivations are evaluated by simulating the backscatter by using spherically focused sources (*f*-numbers of 1, 2, and 4) adjacent to attenuating media (0.05 to 1 dB/cm/MHz) that contain scatterers with Gaussian impedance distributions. The generalized attenuation-compensation function yielded results accurate to 7.2% while the traditional attenuation-compensation functions that neglected focusing had errors as high as 103%. [DOI: 10.1121/1.1757452]

PACS numbers: 43.80.Qf, 43.80.Vj [FD] Pages: 578–593

LIST OF SYMBOLS

a	aperture radius for a spherically focused source.
A_{comp}	generalized attenuation-compensation function including focusing effects along the beam axis.
a_{eff}	effective radius of scatterer.
a_{eff_j}	estimated effective radius of scatterer found from one set (i.e., 25 averaged rf echoes) of simulated backscatter waveforms.
$\overline{a}_{\text{eff}}$	mean value of estimated effective radius from all sets of simulated backscatter waveforms (i.e., $\overline{a}_{\text{eff}}=\Sigma_{\forall j}a_{\text{eff}_j}/\Sigma_{\forall j}j$).
A_{OO}	Oelze–O'Brien attenuation-compensation function.
A_{OM}	O'Donnell–Miller attenuation-compensation function.
A_{PC}	point attenuation-compensation function.
B_γ	correlation function related to field and scatterers.
c	small-signal sound speed of background medium.
F	focal length for a spherically focused source.
f	frequency.
$f\#$	*f*-number for a spherically focused source (i.e., $f\#=F/2a$).
$g(\vec{r}_d,\vec{r}')$	Green's function for the background medium containing the scatterers valid from the detector to the scattering region.
G_o, G_{o_trans}	geometric gain value on receive/transmit for velocity potential field at focus when W_{source} is approximated by a Gaussian (units of m).
G_T	dimensionless aperture gain function that accounts for the focusing of the ultrasound source.
g_{win}	windowing function used to gate the signal.
H	dimensionless filtering characteristics for the ultrasound source.
k	wave number in the scattering region, V' (i.e., $k=2\pi/\lambda$).
$\tilde{k}$	complex wave number of the background about the scatterers (i.e., $\tilde{k}=k+i\alpha$).
k_o	wave number in water.
K_{uV}	conversion constant relating voltage to particle velocity for ultrasound source (units of m/s V^{-1}).
L	total width of rectangular windowing function.
$\overline{n}$	average scatterer number density.
p_{inc}	pressure field incident on the scatterers.
p_s	scattered pressure field.
p_{tot}	total pressure field (i.e., $p_{\text{tot}}=p_s+p_{inc}$).

[a)]Author to whom all correspondence should be addressed. Electronic mail: wdo@uiuc.edu

$\vec{r},\vec{r}',\vec{r}''$ spatial locations in spherical coordinates.
$\Delta\vec{r},\vec{s}$ change of spatial variables [i.e., $\Delta\vec{r}=\vec{r}'-\vec{r}''$ and $\vec{s}=(\vec{r}'+\vec{r}'')/2$].
$\vec{r}_f$ locations on rigid reference plane in spherical coordinates.
$r_{\max}$ upper limit of integration when comparing Gaussian approximation to real source [i.e., $r_{\max}=12.5\cdot 0.51\lambda(f\#)$].
$\vec{r}_T,\vec{r}_d$ locations on aperture plane of transmitter/detector in spherical coordinates.
r_ρ coordinate distance away from beam axis (i.e., $r_\rho=\sqrt{x^2+y^2}$).
$R_{\gamma\gamma}$ autocorrelation function for the scatterer (i.e., $R_{\gamma\gamma}(\Delta\vec{r})=\mathrm{E}[\gamma(\vec{s}+\Delta\vec{r}/2)\gamma(\vec{s}-\Delta\vec{r}/2)]$).
$\Re_{\gamma\gamma}$ power spectral density function for the scatterer.
S_f rigid plane near focal plane used to acquire reference waveform.
S_T aperture area of ultrasound transmitter.
T_{win} total width of rectangular windowing function applied to time-domain waveform (i.e., $T_{win}=2L/c$).
u_z particle velocity perpendicular to aperture plane of ultrasound transmitter/detector.
V' volume containing scatterers contributing to the scattered signal.
V_{inc} voltage applied to the ultrasound source during transmit.
V_{plane} voltage from ultrasound source due to the backscatter from rigid plane near focus.
V_{refl} voltage from ultrasound source due to the backscatter from scatterers.
V_s average scatterer volume.
W_{source} geometric falloff of field intensity in focal region (units of m^2).
w_x,w_y,w_z equivalent Gaussian dimensions on receive of velocity potential field in focal region.
$w_{x\_trans},w_{y\_trans},$ w_{z_trans} equivalent Gaussian dimensions on transmit of velocity potential field in focal region.
z_f distance of rigid plane used to acquire reference waveform to the focal plane.
z_o the shift of the focus away from the theoretical location at a particular frequency.
z_T,z_d distance of aperture plane of the ultrasound transmitter/detector to the focal plane.
z_{trans} distance from transmit focus to receive focus.
α attenuation in the scattering region, V'.
α_{eff} effective attenuation for all tissue between focal plane and aperture plane (i.e., total attenuation along beam axis $=\alpha_{\mathrm{eff}}z_T$).
γ combined perturbation of density and compressibility [i.e., $\gamma(\vec{r})=\gamma_\kappa(\vec{r})-\gamma_\rho(\vec{r})$].
γ_o mean squared variation in acoustic impedance per scatterer.
γ_κ local perturbation in the compressibility due to the scatterers [i.e., $\gamma_\kappa(\vec{r})=[\kappa_s(\vec{r})-\kappa]/\kappa$].
γ_ρ local perturbation in the density due to the scatterers [i.e., $\gamma_\rho(\vec{r})=\rho_s(\vec{r})-\rho/\rho_s(\vec{r})$].
κ compressibility of background medium surrounding scatterers.
κ_s compressibility of scatterers.
ϕ_{real} velocity potential field for real source (i.e., not approximate three-dimensional Gaussian distribution).
λ wavelength.
λ_o the wavelength corresponding to the spectral peak from the reference spectrum (i.e., V_{plane}) used to calculate the depth of focus for the transducer.
ρ density of background medium surrounding scatterers.
ρ_o density of water.
ρ_s density of scatterers.
σ_{lower} percent deviation in values of scatterer size for sizes smaller than the mean size (i.e., $a_{\mathrm{eff}_j}<\overline{a_{\mathrm{eff}}}$).
σ_{upper} percent deviation in values of scatterer size for sizes larger than the mean size (i.e., $a_{\mathrm{eff}_j}>\overline{a_{\mathrm{eff}}}$).
ω radian frequency.

I. INTRODUCTION

One of the distinguishing features of backscattered waveforms returned from biological tissue is the scattering observed within homogeneous tissues between the tissue boundaries. These signals have long been thought to contain information related to the tissue microstructure.[1–6] In order to extract microstructure information, models have been developed to elucidate scattering details. By fitting the measured backscattered data to the model, structural characteristics of the tissue, such as mean scatterer size and acoustic concentration (acoustical impedance of the scatterer multiplied by the number of density scatterers in the region), can be estimated.[4–7] Determining either of these quantities accurately and precisely is hypothesized to improve the diagnostic potential of medical ultrasound by allowing for quantitative measurements to be made of the underlying scattering structure of the tissue that could then be correlated with tumor morphology.[7]

Most of the previous models have assumed plane waves incident on the scattering region (i.e., inside focal zone of weakly focused source) while only considering diffraction effects in the transverse plane.[3–5] Diffraction effects along the beam axis have been neglected. Other authors included a complete Green's function description of the source when determining the scattered field.[8–12] In their calculations, they assumed that the excitation across the entire surface of the source was known or could be accurately determined. They also assumed that the scatterers were a sufficient distance from the source, and the field was approximately constant across the scatterer. Unfortunately, the resulting equations were cumbersome, requiring a precise knowledge of the source's excitation in order to solve for the required fields. As a result, it is difficult to use their results when experimentally calibrating a focused source for the purpose of estimat-

ing scatterer size. Furthermore, their analysis still does not provide analytical insight into the effects of beam diffraction. Recently, Gerig *et al.*[13] proposed using a reference phantom to obtain a reference spectrum that could potentially account for focusing. However, the ability of the reference phantom technique to correct for focusing has not been fully evaluated, and the reference phantom technique still does not provide any analytical insight.

Due to these limitations most investigators only use large *f*-number transducers in their backscatter analyses where diffraction effects along the beam axis can be neglected over the size of the region of interest (i.e., time-gated region). Reducing the length of the time gate to allow for smaller *f*-number transducers is not feasible because both the accuracy and precision of the scatterer size estimates degrade when the window length is too small. This is potentially restrictive in diagnostic imaging systems where smaller *f*-numbers may be desirable to improve the spatial resolution of the parametric image. Hence, the purpose of our work is to allow for the use of focused sources when quantifying the backscattered ultrasound waveforms regardless of the size of the gated region.

In this paper, we re-derive the expected backscattered signal from a region of randomly positioned identical scatterers without the plane wave approximation. Instead, we assume that the velocity potential field near the focus can be accurately modeled as a three-dimensional Gaussian beam while continuing to assume that the scatterers are a sufficient distance from the source, and the field is approximately constant across the scatterer. Then, the validity of the Gaussian approximation of the field is assessed by comparing the approximation to calculations of the velocity potential field from ideal spherically focused sources. Based on our theoretical approximations, we then generate computer simulations to aid in the understanding of the impact of diffraction along the beam axis. Specifically, the computer simulations quantify the effect of varying tissue attenuation as well as assess the accuracy and precision of the scatterer size estimator for a focused source. Simulations are also performed to validate the three-dimensional Gaussian beam approximation for spherically focused sources. Finally, we discuss some of the implications of our results.

II. THEORETICAL DEVELOPMENTS

In this section of the paper, we re-derive the expected backscattered voltage spectrum from a region of randomly positioned uniform scatterers (i.e., same size and shape) and from a rigid plane (a reference) upon being exposed to a focused ultrasound field assuming linear acoustics. The goal of our analysis is to provide insight into the effects of focusing along the beam axis as well as provide useful equations that are easily implemented by future investigators. The coordinate system for our derivations has the origin at the focus of the ultrasound field with the beam axis lying along the z axis and the source positioned at $z_T>0$ (Fig. 1). Although the initial equations can be found in the previously published literature, we have elected to include them in this work because the notation used to denote the variables varies between publications.[4,8,14] In addition, it is critical to the understanding of the derived equations that all of the assumptions made during the derivation be clearly known. Otherwise, the derived equations may not be appropriately applied in the future.

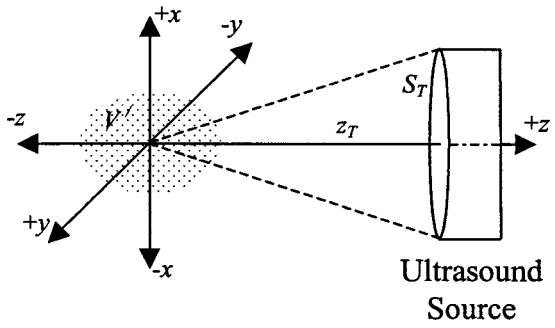

FIG. 1. Coordinate system for theoretical derivations.

A. Derivation of backscattered voltage from scatterers

From a Green's function analysis, it can be shown that the scattered field from the particles at some detector location should be given by[14]

$$p_s(\vec{r}_d)=\int\int_{V'}\int \{\tilde{k}^2\gamma_\kappa(\vec{r}')p_{\text{tot}}(\vec{r}')g(\vec{r}_d,\vec{r}') + \gamma_\rho(\vec{r}')\nabla' p_{\text{tot}}(\vec{r}')\cdot\nabla' g(\vec{r}_d,\vec{r}')\}\,d\vec{r}'. \tag{1}$$

If we assume that the fluctuations in κ and ρ are small throughout the background region, then $g(\vec{r}_d,\vec{r}')$ is approximated by the homogeneous Green's function given by

$$g(\vec{r}_d,\vec{r}')\cong\frac{1}{4\pi}\frac{e^{i\tilde{k}|\vec{r}_d-\vec{r}'|}}{|\vec{r}_d-\vec{r}'|}. \tag{2}$$

To simplify Eq. (1), we assume that the scatterers satisfy the Born approximation,[3,4] so that p_{tot} can be replaced by only the incident field on the scatterers given by[14]

$$p_{inc}(\vec{r}')=-2i\omega\rho\int\int_{S_T} u_z(\vec{r}_T)g(\vec{r}',\vec{r}_T)\,d\vec{r}_T. \tag{3}$$

Substituting Eqs. (2) and (3) into Eq. (1) then yields

$$p_s(\vec{r}_d)=-2i\omega\rho\int\int_{S_T}d\vec{r}_T\int\int_{V'}\int\left\{\begin{matrix}\tilde{k}^2\gamma_\kappa(\vec{r}')u_z(\vec{r}_T)g(\vec{r}',\vec{r}_T)g(\vec{r}_d,\vec{r}')\\ +\gamma_\rho(\vec{r}')u_z(\vec{r}_T)\nabla' g(\vec{r}',\vec{r}_T)\cdot\nabla' g(\vec{r}_d,\vec{r}')\end{matrix}\right\}d\vec{r}'. \tag{4}$$

Equation (4) can be further simplified assuming that the dimensions of the scattering region are small compared to its distance from the source and detector. This can be expressed mathematically as[14]

$$|\vec{r}_T-\vec{r}'|\cong r_T-\frac{\vec{r}_T}{r_T}\cdot\vec{r}',$$
$$|\vec{r}_d-\vec{r}'|\cong r_d-\frac{\vec{r}_d}{r_d}\cdot\vec{r}'. \tag{5}$$

The validity of this approximation increases with decreasing window length used to gate the signal in the time domain (i.e., artificial decrease in the size of the scattering region), with increasing focusing (i.e., decreasing *f*-number), and with increasing focal length. If we also assume that the source and detector are in approximately the same direction (i.e., different elements on the same source so that angle dependence of the backscatter can be neglected), then

$$\left(\frac{\vec{r}_d\cdot\vec{r}_T}{r_d r_T}\right)\approx 1. \tag{6}$$

Similar approximations to those given in Eqs. (5) and (6) were also made by Madsen *et al.*[8] Using these approximations and solving for the gradient of the Green's function results in the scattered pressure field being approximately given by

$$p_s(\vec{r}_d)=(-2i\omega\rho)\left(\frac{\tilde{k}}{4\pi}\right)^2\frac{e^{i\tilde{k}r_d}}{r_d}\int\int_{S_T}d\vec{r}_T \times\left(u_z(\vec{r}_T)\frac{e^{i\tilde{k}r_T}}{r_T}\int\int\int_{V'}d\vec{r}'\,\gamma(\vec{r}')\times e^{-i\tilde{k}\vec{r}'\cdot(\vec{r}_d/r_d\vec{r}_T/r_T)}\right). \tag{7}$$

Now that we know the scattered field within the bounds of our assumptions at some detector location, we need to translate it into the voltage output by the transducer. Hence, we assume that the voltage across the transducer is directly related to the normal particle velocity at the aperture plane according to the relations

$$u_z(\vec{r}_T,\omega)=K_{uV}(\omega)V_{inc}(\omega)G_T(\vec{r}_T,\omega)H(\omega),$$
$$V_{refl}(\omega)=\frac{H(\omega)}{S_T K_{uV}(\omega)}\int\int_{S_T}d\vec{r}_d u_z(\vec{r}_d,\omega)G_T(\vec{r}_d,\omega). \tag{8}$$

The focusing ability of the source (i.e., concavity of the aperture) is captured by the spatially varying complex gain term, $G_T(\vec{r}_T,\omega)$, defined at the aperture plane. Combining Eqs. (7) and (8), while assuming that $z_d\cong r_d$ for amplitude terms, yields

$$V_{refl}(\omega)=\frac{H(\omega)}{i\omega\rho S_T K_{uV}(\omega)}\int\int_{S_T}d\vec{r}_d G_T(\vec{r}_d,\omega)\frac{\partial p_s(\vec{r}_d)}{\partial z_d}$$
$$\cong\frac{V_{inc}(\omega)H^2(\omega)(-2i\tilde{k})(\tilde{k}/4\pi)^2}{S_T}\times\int\int\int_{V'}d\vec{r}'[\gamma(\vec{r}')W_{source}(\tilde{k},\vec{r}')], \tag{9}$$

where

$$W_{source}(\tilde{k},\vec{r}')=\left(\int\int_{S_T}d\vec{r}_T G_T(\vec{r}_T,\omega)\frac{e^{i\tilde{k}r_T-i\tilde{k}\vec{r}'\cdot\vec{r}_T/r_T}}{r_T}\right)^2. \tag{10}$$

Equations (9) and (10) are valid for any source provided that the scattering region is a reasonable distance from the source [i.e., Eqs. (5) and (6) valid]. We can simplify our analysis by assuming that the ultrasound source produces a velocity potential field with a three-dimensional Gaussian distribution. As a result, Eq. (10) can be rewritten as

$$W_{source}(\tilde{k},\vec{r}')\cong(G_o e^{-((x'/w_x(\lambda))^2+(y'/w_y(\lambda))^2+(z'/w_z(\lambda))^2)})^2\times e^{i2\tilde{k}(z_T-z')}. \tag{11}$$

Now that the scattered field at the detector location has been found given a known arrangement of scatterers, $\gamma(\vec{r}')$, the analysis needs to be extended for multiple randomly oriented scatterers. Consider the second moment of the received voltage given by

$$E[V_{refl}(\omega)V^*_{refl}(\omega)]=4\left|\frac{\tilde{k}}{S_T}\right|^2\left|\frac{\tilde{k}}{4\pi}\right|^4|H(\omega)|^4|V_{inc}(\omega)|^2\int\int\int_{V'}d\vec{r}'\left(\int\int\int_{V'}d\vec{r}''\begin{pmatrix}W_{source}(\tilde{k},\vec{r}')W^*_{source}(\tilde{k},\vec{r}'')\\ E[\gamma(\vec{r}')\gamma(\vec{r}'')]\end{pmatrix}\right)$$
$$=4G_o^4\left|\frac{\tilde{k}}{S_T}\right|^2\left|\frac{\tilde{k}}{4\pi}\right|^4|H(\omega)|^4|V_{inc}(\omega)|^2e^{-4\alpha_{\text{eff}}z_T}\int\int\int_{V'}d\vec{r}' \times\left(\int\int\int_{V'}d\vec{r}''\begin{pmatrix}e^{-2(((x'^2+x''^2)/w_x^2)+((y'^2+y''^2)/w_y^2)+((z'^2+z''^2)/w_z^2))}\\ E[\gamma(\vec{r}')\gamma(\vec{r}'')]e^{-2ik(z'-z'')+2\alpha(z'+z'')}\end{pmatrix}\right), \tag{12}$$

where "*" is the complex conjugate and E[~] denotes expected value.[15] If we then perform the change of variables letting $\Delta\vec{r}=\vec{r}'-\vec{r}''$ and $\vec{s}=(\vec{r}'+\vec{r}'')/2$ as was done by Insana *et al.*,[4] Eq. (12) becomes

$$\mathrm{E}[|V_{refl}(\omega)|^2]=4G_o^4\left|\frac{\tilde{k}}{S_T}\right|^2\left|\frac{\tilde{k}}{4\pi}\right|^4|H(\omega)|^4|V_{inc}(\omega)|^2 \times \mathrm{e}^{-4\alpha_{\mathrm{eff}}z_T}\int\int_{V'}\int d\Delta\vec{r} \times(\mathrm{e}^{-((\Delta r_x^2/w_x^2)+(\Delta r_y^2/w_y^2)+(\Delta r_z^2/w_z^2))} \times \mathrm{e}^{-2ik\Delta r_z}B_\gamma(\Delta\vec{r})), \quad (13)$$

where

$$B_\gamma(\Delta\vec{r})=\int\int_{V'}\int d\vec{s}\left(\mathrm{E}\left[\gamma\left(\vec{s}+\frac{\Delta\vec{r}}{2}\right)\gamma\left(\vec{s}-\frac{\Delta\vec{r}}{2}\right)\right] \times \mathrm{e}^{-4((s_x^2/w_x^2)+(s_y^2/w_y^2)+(s_z^2/w_z^2))}e^{4\alpha s_z}\right). \quad (14)$$

Equation (14) can be further simplified by making some reasonable assumptions about the scatterers. If γ is weakly stationary within the scattering volume, then the autocorrelation function $E[\gamma(\vec{s}+\Delta\vec{r}/2)\gamma(\vec{s}-\Delta\vec{r}/2)]$ depends only on the separation between the points being correlated, $\Delta\vec{r}$, and is negligible for $\Delta\vec{r}$ larger than the size of the scatterers.[4] Furthermore, because the scatterers are typically much smaller than the focal dimensions, we can make the approximation that the amplitude of the field is constant across each individual scatterer, or $\mathrm{e}^{-((\Delta r_x^2/w_x^2)+(\Delta r_y^2/w_y^2)+(\Delta r_z^2/w_z^2))}\approx 1$, an approximation also made by Madsen *et al.*[8] This approximation restricts our theory to subresolution scatterers. Lastly, if we assume that the beam width in the focal plane (i.e., w_x and w_y) is much smaller than the width of the scattering region so that the integration in the focal plane can be extended to infinity, then Eq. (13) becomes

$$E[|V_{refl}(\omega)|^2]=4G_o^4\left|\frac{\tilde{k}}{S_T}\right|^2\left|\frac{\tilde{k}}{4\pi}\right|^4|H(\omega)|^4|V_{inc}(\omega)|^2\mathrm{e}^{-4\alpha_{\mathrm{eff}}z_T}\left(\begin{array}{l}\int\int_{V'}\int d\Delta\vec{r}(\mathrm{e}^{-2ik\Delta r_z}R_{\gamma\gamma}(\Delta\vec{r}))\\ \int\int_{V'}\int d\vec{s}(\mathrm{e}^{-4((s_x^2/w_x^2)+(s_y^2/w_y^2)+(s_z^2/w_z^2))}\mathrm{e}^{4\alpha s_z})\end{array}\right)$$

$$=4G_o^4\left|\frac{\tilde{k}}{S_T}\right|^2\left|\frac{\tilde{k}}{4\pi}\right|^4|H(\omega)|^4|V_{inc}(\omega)|^2\mathrm{e}^{-4\alpha_{\mathrm{eff}}z_T}\Re_{\gamma\gamma}(2k\hat{z})\left(\frac{w_xw_y\pi}{4}\right)\left(\int_{V'}ds_z\mathrm{e}^{-4(s_z^2/w_z^2)}\mathrm{e}^{4\alpha s_z}\right), \quad (15)$$

where, for Gaussian spheres and spherical shells, $\Re_{\gamma\gamma}$ is given by[4]

$$\Re_{\gamma\gamma}(2k\hat{z})=\begin{cases}\overline{n}V_s^2\gamma_o^2\left[\dfrac{\sin(2ka_{\mathrm{eff}})}{2ka_{\mathrm{eff}}}\right]^2 & (Shell),\\ \overline{n}V_s^2\gamma_o^2\mathrm{e}^{-0.827k^2a_{\mathrm{eff}}^2} & (Gaussian).\end{cases} \quad (16)$$

At this point, we can consider the effects of windowing in the time domain. Windowing, to a first-order approximation, causes a blurring (i.e., convolution) of the spectrum in the frequency domain and eliminates the contribution of scatterers a distance from the focus greater than the window length along the beam axis (i.e., the s_z integration). The impact of the convolution on the estimate of scatterer size is only significant at small window lengths as has been addressed by previous authors.[16] As a result, we will only consider the elimination of scatterers by the window. Hence, Eq. (15) becomes

$$\mathrm{E}[|V_{refl}(\omega)|^2]=\frac{4G_o^4|\tilde{k}|^6|H(\omega)|^4|V_{inc}(\omega)|^2}{(4\pi)^4S_T^2A_{comp}(\omega)}\left(\frac{w_xw_y\pi}{4}\right) \times\Re_{\gamma\gamma}(2k\hat{z}), \quad (17)$$

where

$$A_{comp}(\omega)=\frac{\mathrm{e}^{4\alpha_{\mathrm{eff}}z_T}}{(\int_{-L/2}^{L/2}ds_z\,g_{win}(s_z)\mathrm{e}^{-4(s_z^2/w_z^2)}\mathrm{e}^{4\alpha s_z})}. \quad (18)$$

Equations (17) and (18) are applicable for any type of windowing function, g_{win}, and Eq. (18) is a generalized attenuation-compensation function that includes attenuation, windowing, and focusing. If, for example, we let $w_z\to\infty$ (i.e., remove focusing along the beam axis) and use a rectangular windowing function, then Eq. (18) becomes

$$A_{OM}(\omega)=\frac{4\alpha\mathrm{e}^{4\alpha_{\mathrm{eff}}z_T}}{\mathrm{e}^{4\alpha L/2}-\mathrm{e}^{-4\alpha L/2}}, \quad (19)$$

which is the O'Donnell–Miller attenuation-compensation

function.[17] Hence, the O'Donnell–Miller attenuation-compensation function neglects the natural falloff of the field, increasing the evaluation of the integral in Eq. (18) and subsequently undercompensating for the attenuation. As a result, O'Donnell–Miller compensation should result in an overestimate of the scatterer size because the values at higher frequencies are smaller than they should be due to the uncompensated attenuation. Likewise, if we neglect all field variations in the scattering region, Eq. (18) becomes

$$A_{PC}(\omega)=\frac{e^{4\alpha_{\text{eff}}z_T}}{L}, \tag{20}$$

which is the point compensation.[18] Point compensation will either under- or overestimate the scatterer size depending upon the relative importance of diffraction (w_z term) and attenuation (α term) due to the sign difference in the integrand of Eq. (18).

In our derivation of Eqs. (17) and (18), we assumed that the transmit and receive foci were at the same location. In diagnostically relevant fields, however, the two foci often occur at different locations due to the smaller number of foci used on transmit. When the two foci are at different locations, Eq. (11) becomes

$$W_{source}(\tilde{k},\vec{r}\,')\cong(G_o e^{-((x'/w_x)^2+(y'/w_y)^2+(z'/w_z)^2)})(G_{o\_trans}e^{-((x'/w_{x\_trans})^2+(y'/w_{y\_trans})^2+(z'-z_{trans})/w_{z\_trans})^2})e^{i2\tilde{k}(z_T-z')}. \tag{21}$$

As a result, Eqs. (17) and (18) become

$$\mathrm{E}[|V_{refl}(\omega)|^2]=\frac{2G_{o\_trans}^2G_o^2|\tilde{k}|^6|H(\omega)|^4|V_{inc}(\omega)|^2}{(4\pi)^4S_T^2A_{comp}(\omega)}\times\left(\frac{\pi w_x w_{x\_trnas}w_y w_{y\_trans}}{\sqrt{(w_{x\_trans}^2+w_x^2)(w_{y\_trans}^2+w_y^2)}}\right)\times\Re_{\gamma\gamma}(2k\hat{z}) \tag{22}$$

and

$$A_{comp}(\omega)=\frac{e^{4\alpha_{\text{eff}}z_T}}{(\int_{-L/2}^{L/2}ds_z g_{win}(s_z)e^{-2(s_z^2/w_z^2+(s_z-z_{trans})^2/w_{z\_trans}^2)+4\alpha s_z})}. \tag{23}$$

Hence, our analysis can be easily extended to diagnostically relevant fields even though we restrict our attention to sources with a single transmit and receive focus in the remainder of this paper.

B. Derivation of backscattered voltage from rigid plane near focus

In this section, we derive the received voltage for scattering sound off of a rigid plane located near the focal plane due to its popularity as a method for obtaining a reference.[3,4,6,8] We can solve for the received voltage by treating the reflected field at the rigid plane as a virtual source. Hence, the reflected field at the aperture of the transducer is given by

$$p_{plane}(\vec{r}_d,\omega)=-2i\omega\rho_o\int\int_{S_f}d\vec{r}_f u_z(\vec{r}_f)\frac{e^{ik_o r_d}}{4\pi r_d}e^{-ik_o(\vec{r}_d/r_d)\vec{r}_f}, \tag{24}$$

where

$$u_z(\vec{r}_f)=\frac{-2ik_oK_{uV}(\omega)V_{inc}(\omega)H(\omega)}{4\pi}\int\int_{S_T}d\vec{r}_T G_T(\vec{r}_T,\omega)\times\frac{e^{ik_o r_T-ik_o\vec{r}_f\cdot(\vec{r}_T/r_T)}}{r_T}. \tag{25}$$

As a result, the received voltage detected by the source is given by

$$V_{plane}(\omega)=\frac{-4k_o^2V_{inc}(\omega)H^2(\omega)}{S_T(4\pi)^2}\int\int_{S_f}d\vec{r}_f\times\left(\int\int_{S_T}d\vec{r}_d G_T(\vec{r}_d,\omega)\frac{e^{ik_o r_d-ik_o\vec{r}_f\vec{r}_d/r_d}}{r_d}\right)^2. \tag{26}$$

Likewise, if we again assume the velocity potential field near the focus has a three-dimensional Gaussian distribution, then Eq. (26) becomes

$$\begin{aligned}V_{plane}(\omega)&=\frac{-4k_o^2V_{inc}(\omega)H^2(\omega)}{S_T(4\pi)^2}e^{i2k_o(z_T-z_f)}e^{-2(z_f/w_z)^2}\times\int\int_{S_f}d\vec{r}_f(G_o e^{-(x_f/w_x)^2-(y_f/w_y)^2})^2\\&=\frac{-2\pi w_x w_y k_o^2G_o^2V_{inc}(\omega)H^2(\omega)}{S_T(4\pi)^2}\times e^{i2k_o(z_T-z_f)}e^{-2(z_f/w_z)^2}.\end{aligned} \tag{27}$$

Based on Eq. (27), the expected normalized backscatter is then given by

$$\frac{\mathrm{E}[|V_{refl}(\omega)|^2]}{|V_{plane}(\omega)|^2} = \frac{|\tilde{k}|^6 \mathrm{e}^{4(z_f/w_z)^2}}{4\pi w_x w_y k_o^4} \frac{\Re_{\gamma\gamma}(2k\hat{z})}{A_{comp}(\omega)}$$

$$\propto k_o^4 \mathrm{e}^{4(z_f/w_z)^2} \frac{\Re_{\gamma\gamma}(2k\hat{z})}{A_{comp}(\omega)}, \tag{28}$$

where the k_o^4 dependence results from both w_x and w_y being proportional to λ. Equation (28) can then be solved to yield the scatterer size, given that the form of $\Re_{\gamma\gamma}$ is known, using standard techniques that minimize the squared error in the log domain assuming that both the sound speed and the attenuation of the medium are known.[4] Notice that focusing along the beam axis introduces the error term $\mathrm{e}^{4z_f^2/w_z^2}$ whenever the plane is not placed exactly at the focus. However, the experimental error in positioning the plane also scales with w_z, so there is no calibration advantage in using larger *f*-number transducers.

III. VALIDATION OF GAUSSIAN APPROXIMATION

The theoretical derivations in the previous section were simplified by assuming that the velocity potential field for a focused source could be accurately approximated by a three-dimensional Gaussian in the focal region. However, the validity of this approximation needs to be addressed before the derived generalized attenuation-compensation function can be applied. In this section of the paper, the Gaussian approximation is compared to a complete velocity potential field (i.e., complete field) as computed from an established code.[19] The complete field was calculated for spherically focused transducers with *f*-numbers of 1, 2, and 4 and diameters of 5, 2.5, and 1.25 cm, respectively, at frequencies from 2 to 14 MHz in steps of 1 MHz. For each source at each frequency, the field was calculated on a rectangular grid corresponding to a single slice through the cylindrically symmetric field extending from 4 to 6 cm from the aperture plane of the source along the beam axis (theoretical focal length for all sources was 5 cm) and radially 2 cm off of the beam axis using a grid spacing of 10 μm. The medium in which the field was calculated was lossless and had a sound speed of 1540 m/s.

After calculating the complete field for each source at each frequency, the Gaussian approximation was compared to the complete field by calculating the percent difference as given by

$$\%Difference = 100 \cdot \frac{\int_{-L/2}^{L/2}\int_0^{r_{\max}}((\phi_{real}(\lambda)/\max(\phi_{real}(\lambda_o)))^2 - e^{-2((r'_\rho/w_x(\lambda))^2+(z'/w_z(\lambda))^2)})^2 r'_\rho\, dr'_\rho\, dz'}{\int_{-L/2}^{L/2}\int_0^{r_{\max}}(\phi_{real}(\lambda)/\max(\phi_{real}(\lambda_o)))^4 r'_\rho\, dr'_\rho\, dz'}, \tag{29}$$
V' V'

where the limits of integration were set by using a window length of $L=13$ mm and $r_{\max}=12.5\cdot 0.51\lambda(f\#)$ for each source and frequency. Also, λ_o was the wavelength corresponding to 8 MHz, and the "focus" at which the Gaussian approximation was centered (i.e., $x'=y'=z'=0$) was defined to be location at which $\phi_{real}(\lambda_o)$ was maximum for each source. Notice that $r_{\max}$ is 12.5 times the -3 dB radius of the beam intensity in the focal plane[20] for each frequency. The values of w_x (same as w_y for cylindrically symmetric sources) and w_z used in Eq. (29) for the Gaussian approximation were given by

$$w_x = w_y = 0.87\lambda f\#, \tag{30}$$

$$w_z = 6.01\lambda(f\#)^2.$$

Equations (30) result from matching the -3 dB transmit beamwidth as given by Kino [20] (i.e., $1.02\lambda f\#$ and $7.08\lambda f\#^2$) to the corresponding Gaussian beamwidth as was done for $w_{x,y}$ by Barber.[21]

The double integral in Eq. (29) was evaluated using the double integration function in MATLAB based on the adaptive-recursive Newton-Cotes eight-panel rule where ϕ_{real} values away from the grid points were linearly extrapolated from the closest grid values. In addition to calculating the percent differences according to Eq. (29), the percent differences were also calculated from

$$\%Difference = 100 \cdot \frac{\int_{-L/2}^{L/2}((\phi_{real}(\lambda)/\max(\phi_{real}(\lambda_o)))^2 - e^{-2(z'/w_z(\lambda))^2})^2\, dz'}{\int_{-L/2}^{L/2}(\phi_{real}(\lambda)/\max(\phi_{real}(\lambda_o)))^4\, dz'}, \tag{31}$$
V' V'

also using an L of 13 mm due to the importance of Gaussian approximation of the field along the beam axis in the equation for the generalized attenuation-compensation function.

The percent differences from Eqs. (29) and (31) for all three sources at each frequency are given in Fig. 2. The percent differences calculated over the entire field [i.e., from Eq. (29)] are always less than 18.75%, indicating that assuming the velocity potential field is a three-dimensional Gauss-

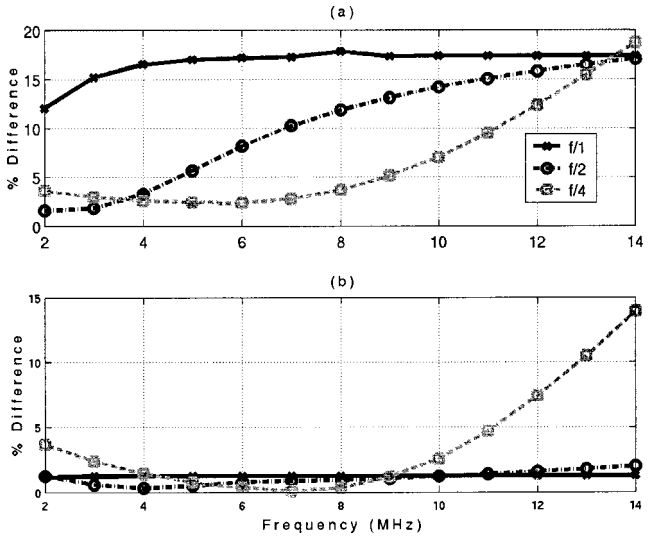

FIG. 2. The percent differences between the complete field and the Gaussian approximation for spherically focused transducers with *f*-numbers of 1, 2, and 4 for frequencies from 2 to 14 MHz calculated using (a) Eq. (29) and (b) Eq. (31).

ian distribution is a reasonable approximation. However, before concluding, the differences between the real and Gaussian fields were explored in greater detail. The percent differences calculated from Eqs. (29) and (31) both exhibit a large increase after a frequency of 8 MHz for the $f/4$ transducer. However, the percent differences from both equations for the $f/1$ transducer are relatively constant with frequency with the results from Eq. (29) plateauing at ~18%. Likewise, the percent differences for the $f/2$ transducer as given by Eq. (29) also seem to approach a plateau of ~18% while the percent differences from Eq. (31) are relatively constant with frequency. Hence, the percent differences for the $f/4$ transducer are probably related to errors in the approximation along the beam axis, z axis, whereas the differences for the $f/1$ and $f/2$ transducers are probably more related to other errors in the approximation (i.e., possibly side lobes).

In order to investigate the errors in the approximation in greater detail, the normalized complete field intensity [i.e., $(\phi_{real}(\lambda)/\max_{V'}(\phi_{real}(\lambda_o)))^2$] and the accompanying Gaussian approximation were plotted for the beam axis (i.e., z axis) and the beamwidth axis (i.e., r_ρ axis) for each of the transducers for frequencies of 4, 8, and 12 MHz as shown in Figs. 3, 4, and 5. For all three transducers and all three frequencies, the Gaussian approximation is in good agreement with the complete field intensity along the beamwidth axis with only a slight discrepancy in the peak value for the $f/4$ transducer at 4 and 12 MHz. Likewise, the agreement is good along the beam axis for the $f/2$ and $f/1$ transducers for all three frequencies as well as for the $f/4$ transducer at 8 MHz. However, the Gaussian approximation differs significantly from the complete field for the $f/4$ transducer at frequencies of 4 and 12 MHz. The discrepancy for the $f/4$ transducer is due to the location of the maximum field intensity (i.e., focus) changing with transmitted frequency whereas the basic Gaussian approximation assumes that the location is independent of frequency. The effects of the shift of the focus are more pronounced at the higher frequency [i.e., Fig. 5(c)] due to the smaller depth of focus. In addition, the shift of the focus is also responsible for the change in the maximum value of field intensity (i.e., G_o^2) with frequency because matching the peak intensities for the real and Gaussian approximation results in an ideal G_o given by

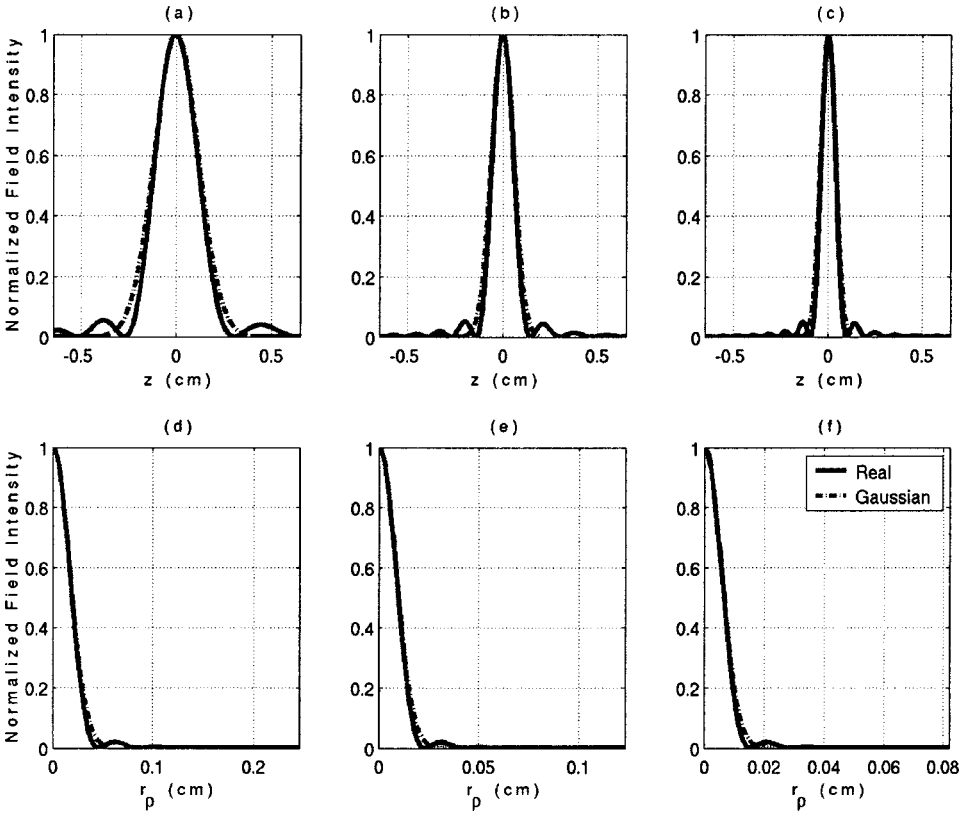

FIG. 3. Plots showing the normalized complete field intensity with the accompanying Gaussian approximation for the z axis at frequencies of (a) 4 MHz, (b) 8 MHz, and (c) 12 MHz as well as the r_ρ axis at frequencies of (d) 4 MHz, (e) 8 MHz, and (f) 12 MHz for an $f/1$ spherically focused transducer.

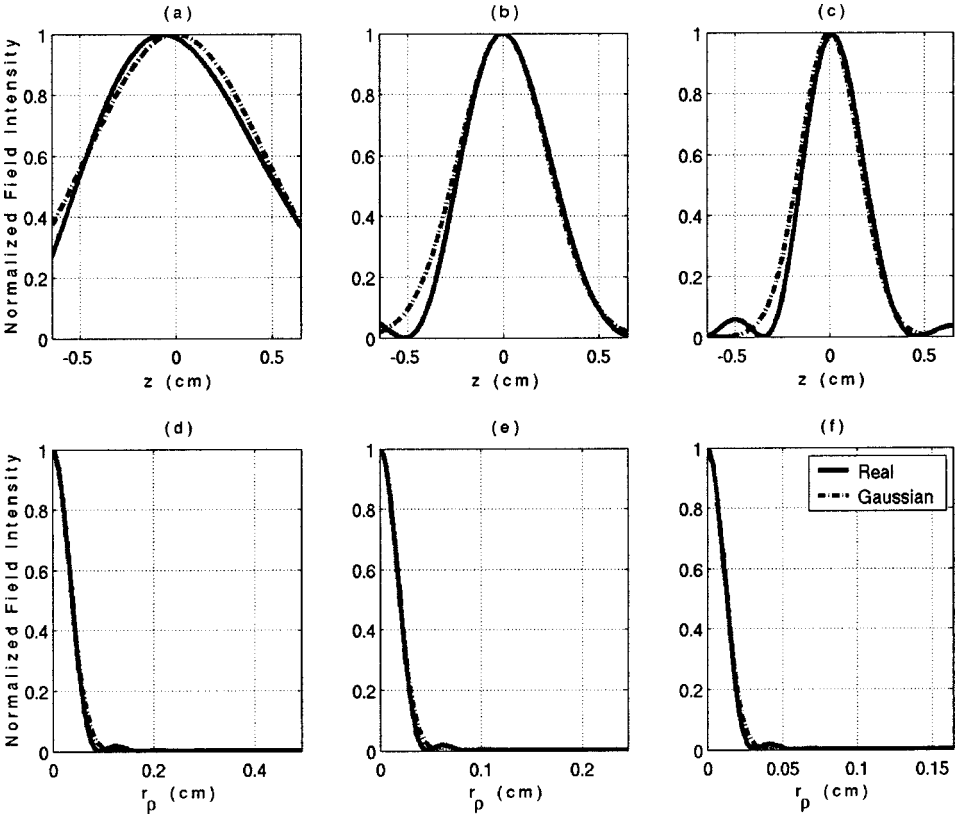

FIG. 4. Plots showing the normalized complete field intensity with the accompanying Gaussian approximation for the z axis at frequencies of (a) 4 MHz, (b) 8 MHz, and (c) 12 MHz as well as the r_ρ axis at frequencies of (d) 4 MHz, (e) 8 MHz, and (f) 12 MHz for an $f/2$ spherically focused transducer.

$$G_o = \frac{a^2}{2F}. \tag{32}$$

Having identified the shifts of the focus with frequency for the weakly focused source, the next step is to determine if the Gaussian approximation could be improved by properly accounting for the shift. Because the shift is always along the beam axis, the integral along ds_z in Eq. (15) could be modified to yield

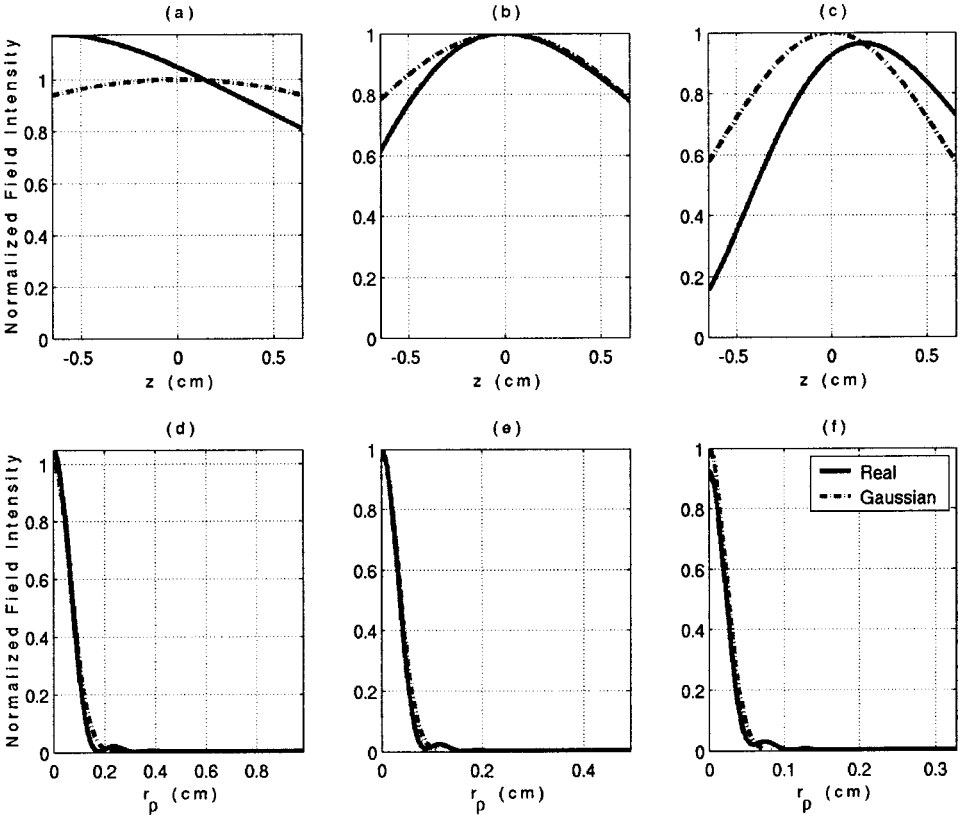

FIG. 5. Plots showing the normalized complete field intensity with the accompanying Gaussian approximation for the z axis at frequencies of (a) 4 MHz, (b) 8 MHz, and (c) 12 MHz as well as the r_ρ axis at frequencies of (d) 4 MHz, (e) 8 MHz, and (f) 12 MHz for an $f/4$ spherically focused transducer.

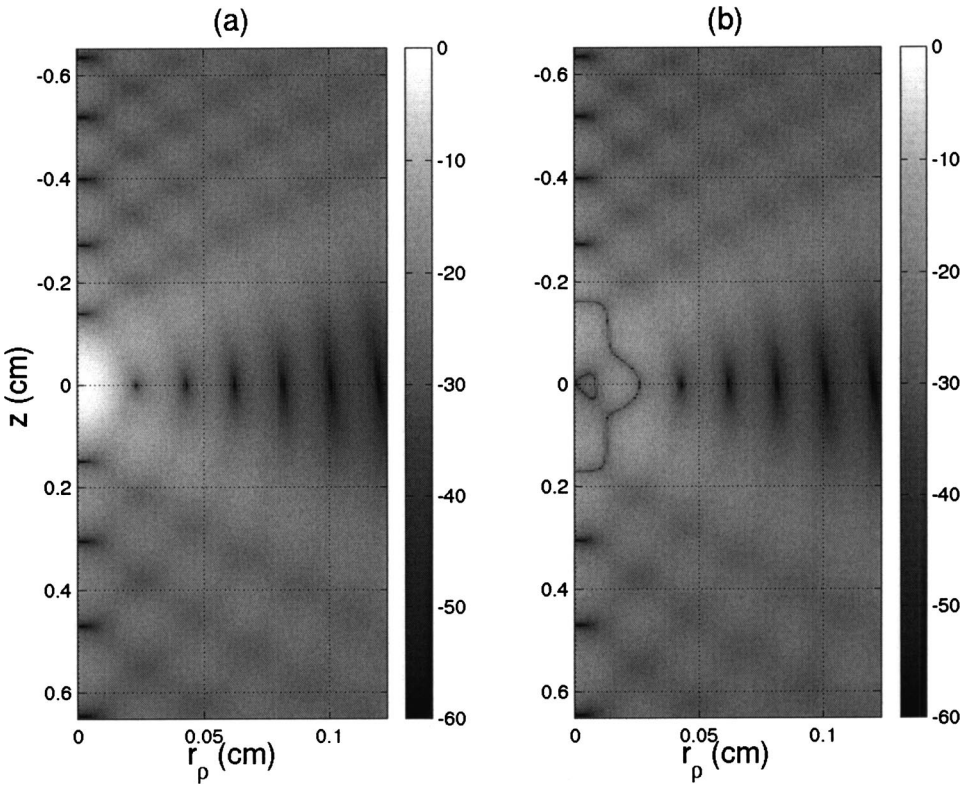

FIG. 6. Images showing (a) the calculated field intensities in dB and (b) the difference term from the integrand in Eq. (29) also in dB for the real $f/1$ source at a frequency of 8 MHz over the integration region.

$$\int_{-L/2}^{L/2} ds_z (g_{win}(s_z) e^{-4(s_z - z_o(f))^2/w_z^2} e^{4\alpha s_z})$$

$$= \int_{-L/2}^{L/2} ds_z (g_{win}(s_z) e^{-4s_z^2/w_z^2 + 8s_z z_o(f)/w_z^2 - 4z_o^2(f)/w_z^2} e^{4\alpha s_z})$$

$$= e^{-4z_o^2(f)/w_z^2} \int_{-L/2}^{L/2} ds_z (g_{win}(s_z) e^{-4s_z^2/w_z^2} \times e^{(4\alpha + 8z_o(f)/w_z^2)s_z}), \quad (33)$$

where z_o is the shift of the focus at a particular frequency. However, the shift of the focus is typically much smaller than w_z. Hence, the terms involving z_o can be ignored, resulting in the same generalized attenuation-compensation function given in Eq. (18). Therefore, the Gaussian approximation could be improved for weakly focused sources provided the equivalent Gaussian depth of focus is found by an independent fit to a Gaussian distribution for every frequency of interest while allowing the peak of the Gaussian to occur at different spatial locations for each frequency.

Now that the percent differences for the weakly focused $f/4$ source have been analyzed, the percent differences for the $f/1$ and $f/2$ sources can be explored in greater detail. The calculated field intensities in dB [i.e., $10 \cdot \log_{10}((\phi_{real}(\lambda)/\max_{V'}(\phi_{real}(\lambda_o)))^2)$] for the real $f/1$ source at a frequency of 8 MHz is shown with the difference term from the integrand in Eq. (29) [i.e., $10 \cdot \log_{10}(|(\phi_{real}(\lambda)/\max_{V'}(\phi_{real}(\lambda_o)))^2 - e^{-2((r'_\rho/w_x(\lambda))^2 + (z'/w_z(\lambda))^2)}|)$] also in dB over the integration region in Fig. 6. Likewise, the calculated field intensities and difference term for the $f/2$ source at frequency of 4 MHz are shown in Fig. 7. Notice that the largest differences between the complete fields and Gaussian approximations in Fig. 6 [i.e., (b) image] result from the "V" shaped side lobe structure before and after the focal plane. When very little of this side lobe structure is included in the integration region (Fig. 7), the corresponding percent difference in Fig. 2(a) is 3.3%. However, when all of the "V" is included in the integration region (Fig. 6), the corresponding percent difference in Fig. 2(a) is close to 18%. Hence, the side lobe structure reduces the accuracy of the Gaussian approximation for focused sources up to a percent difference of ~18%. One way to improve the agreement between the complete fields and Gaussian approximation for focused sources is to use smaller window lengths to gate the time domain signal so that not all of the "V" shaped side lobe structure would influence the backscattered power spectrum.

Before concluding, we need to take another look at the equivalent Gaussian dimensions given in Eq. (30). Although Barber showed that $w_{x,y}$ in Eq. (30) is a good approximation to the real beamwidth for the ideal transducer,[21] the expression for w_z has not been validated. Hence, we tested the equation for w_z by fitting a Gaussian distribution to the calculated complete field intensities along the beam axis for the $f/1$, $f/2$, and $f/4$ sources at each frequency independently (i.e., location of focus along beam axis was allowed to change for the different frequencies). The Gaussian fit was done for a window length of 13 mm about the location of maximum field intensity as measured at a frequency of 8 MHz for all of the frequencies from 2 to 14 MHz except for the $f/4$ source where the Gaussian fit was only done from 4 to 14 MHz due to the real focus shifting outside of the 13 mm window. The difference for the w_z from the fit and the w_z from Eq. (30) was always less than 11.5% for the $f/1$, 6.5% for the $f/2$, and 21.1% for the $f/4$. Also, the w_z values from the Gaussian fit at each frequency could be fit by line

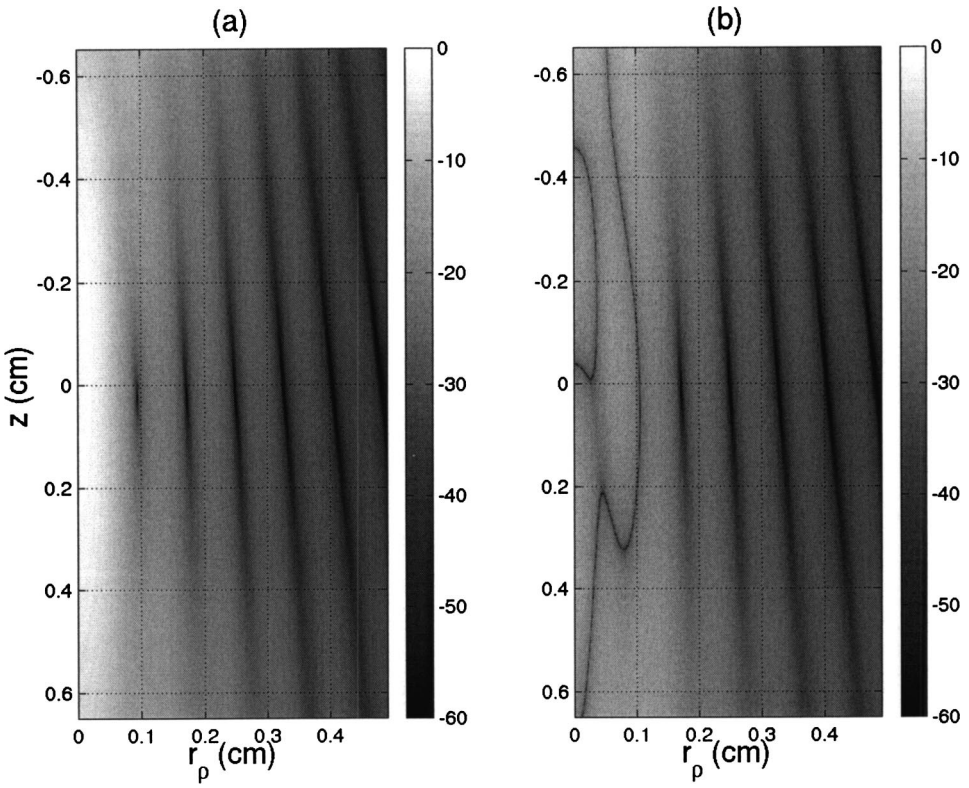

FIG. 7. Images showing (a) the calculated field intensities in dB and (b) the difference term from the integrand in Eq. (29) also in dB for the real $f/2$ source at a frequency of 4 MHz over the integration region.

for each transducer, yielding a wavelength dependence of $5.43\lambda + 15.5\ \mu$m for the $f/1$ [Eq. (30) predicts 6.01λ], $23.1\lambda - 37.2\ \mu$m for the $f/2$ [Eq. (30) predicts 24.0λ], and $84.1\lambda - 503\ \mu$m for the $f/4$ [Eq. (30) predicts 96.2λ]. Hence, the equivalent Gaussian dimensions in Eq. (30) are reasonable first-order approximations for the real ideal focused source.

IV. SIMULATION ANALYSIS

In Sec. II of this paper, we re-derived the backscattered voltage from a region of homogeneous scatterers and from a rigid plane placed near the focus. Based on these equations, we were able to conclude that focusing along the beam axis can be corrected by using a generalized attenuation-compensation function. We also concluded that for focused sources, O'Donnell–Miller compensation should result in an overestimate of the scatterer size, and point compensation may either over- or underestimate the scatterer size depending on the degree of focusing and amount of attenuation. However, the overall estimation performance has not been quantified. Therefore, a series of simulations was performed to quantify the performance of the different attenuation-compensation functions similar to the study done by Oelze and O'Brien.[18] In their work, they introduced a new attenuation-compensation function given by

$$A_{OO}(\omega) = \frac{e^{4\alpha_{\text{eff}} z_T} e^{-4\alpha L/2}}{L} \left(\frac{2\alpha L}{1 - e^{-2\alpha L}} \right)^2, \tag{34}$$

which they found underestimated the scatterer size for the unfocused source. Therefore, their attenuation-compensation function was also considered in our analysis. A_{OO} cannot be derived from Eq. (18) because our derivation dealt with the $E[|V_{refl}(\omega)|^2]$ whereas A_{OO} was originally derived for $(E[|V_{refl}(\omega)|])^2$.

In the simulations, the sources were spherically focused transducers with their apertures placed in contact with an attenuating infinite half-space (infinite region bounded by aperture plane of source) containing scatterers. The transducers were excited by an impulse spike, and the dimensionless filtering characteristics for the ultrasound source, $H(f)$, from Eq. (8) were given by

$$H(f) = \frac{f \cdot \exp(-((f - 8\ \text{MHz})/6\ \text{MHz})^2)}{\max_{\forall f}(f \cdot \exp(-((f - 8\ \text{MHz})/6\ \text{MHZ})^2))}, \tag{35}$$

which was comparable to a single element transducer in our lab. A Rayleigh distribution was selected over a Gaussian distribution so that nothing would be transmitted at zero frequency similar to the filtering characteristics of a real source. Also, the sources had a focal length of 5 cm and *f*-numbers of 1, 2, and 4. The velocity potential field at the focus in the simulations followed a three-dimensional Gaussian distribution (i.e., only approximation of field for focused source) with G_o, w_x, w_y, and w_z given by Eqs. (32) and (30), respectively.

The backscattered voltage for the simulations was generated by solving Eq. (9) analytically for a single Gaussian scatterer at an arbitrary location in the Gaussian field of the focal region. The backscatter for many scatterers in the half-space was then obtained by adding together the backscatter from many different randomly distributed scatterers. In the simulations, the scatterers were positioned according to a uniform probability distribution throughout the focal region

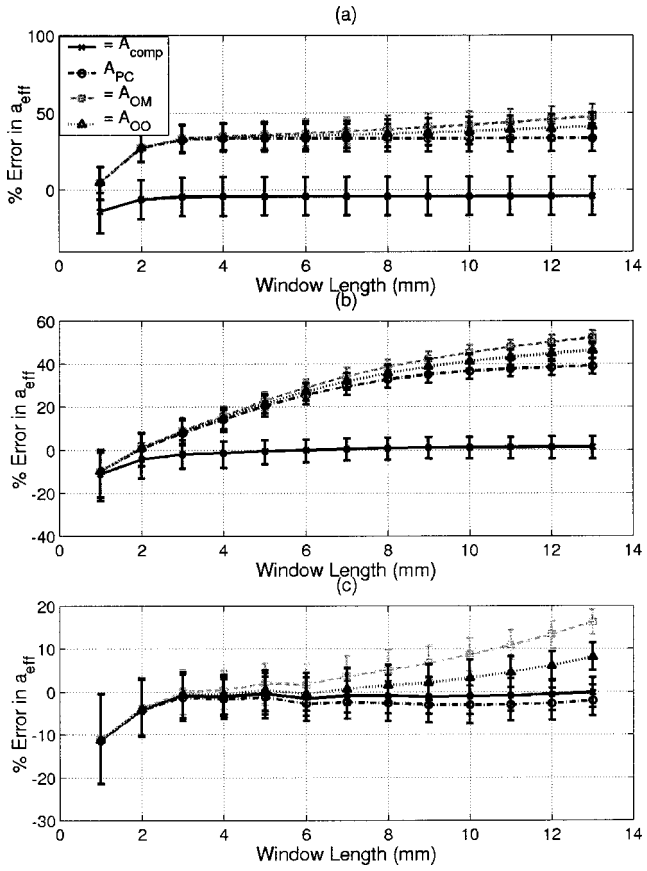

FIG. 8. The % error versus rectangular window length when compared to known a_{eff} at $\alpha=0.5$ dB/cm/MHz for simulated fields from (a) $f/1$, (b) $f/2$, and (c) $f/4$ transducers for each of the attenuation-compensation functions (A_{comp}, A_{PC}, A_{OM}, and A_{OO}).

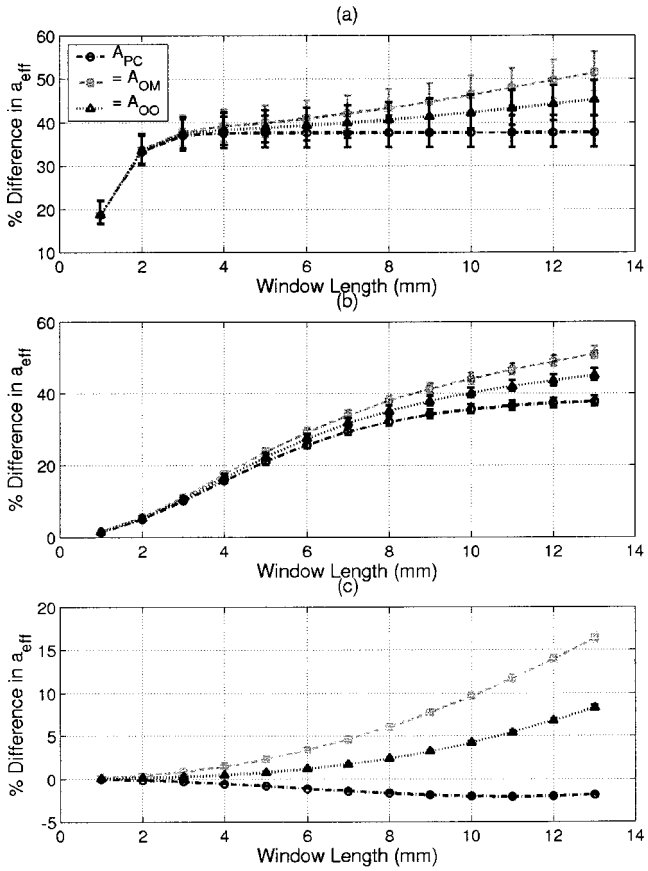

FIG. 9. The % difference between a_{eff} found using the traditional attenuation-compensation functions (A_{PC}, A_{OM}, and A_{OO}) when compared to a_{eff} found using A_{comp} in Eq. (26) versus rectangular window length at $\alpha=0.5$ dB/cm/MHz for simulated fields from (a) $f/1$, (b) $f/2$, and (c) $f/4$ transducers.

at a density of 35/mm^3 and each had an effective radius, a_{eff}, of 25 μm.

A density of 35/mm^3, given that the approximate length of the transmitted pulse was 0.286 mm, translates to 4.8, 1.2, and 0.3 scatterers per resolution cell in the B-mode image for the $f/4$, $f/2$, and $f/1$, respectively. Hence, the speckle would not be fully developed in a B-mode image from the $f/1$ and $f/2$ transducers. This is of little concern because we are not analyzing the speckle, but rather the frequency spectrum of the backscattered signal. As a result, we do not need fully developed speckle to perform our analysis. To verify this assertion, we varied the number density of the scatterers from 35/mm^3 to 3500/mm^3 for the $f/1$ transducer. The accuracy of the scatterer size estimates was the same for all of the number densities ($\sim$1%). The precision of the estimates was improved for larger number densities (from $\sim$26% to $\sim$15%), but the amount of improvement did not warrant an increase in the number density for the simulations.

The sound speed for the half-space was 1532 m/s, which is the sound speed for liver (characteristic of tissue). The attenuation was uniform throughout the half-space for each simulation and was varied from 0.05 to 1 dB/cm/MHz for different simulations. The reflection off of the rigid plane at the focus in a water bath was also simulated according to Eq. (27) using a constant sound speed of 1540 m/s and setting $z_f=0$. The code used a sampling rate of 53 MHz when "digitizing" the signal significantly oversampling the waveform, and no electronic noise was added to the simulated waveforms.

For each value of attenuation, the backscattered voltage (i.e., rf echo) from 1000 independent random scatter distributions was generated. The waveforms were then separated into 40 independent sets with 25 waveforms per set and windowed in the time domain using a rectangular gating function centered at the focus. The width of the rectangular window was varied from 1 to 13 mm in steps of 1 mm with corresponding time gates found from $T_{win}=2L/c$. Then, $\mathrm{E}[|V_{refl}(\omega)|^2]$ was calculated by averaging the magnitude squared of the frequency spectrum of the 25 signals. Equation (28) was then solved by minimizing the squared error using standard techniques[4] in the log domain yielding 40 independent estimates of the effective scatterer radius, a_{eff_j}. In all cases, the bandwidth selected for the minimization was the set of frequencies for which

$$\frac{k_o^4 \mathrm{e}^{-4\alpha z_T}|V_{plane}(\omega)|^2}{\max\limits_{\forall\omega}(k_o^4 \mathrm{e}^{-4\alpha z_T}|V_{plane}(\omega)|^2)} > 0.05. \tag{36}$$

The results for an attenuation of 0.5 dB/cm/MHz for all three transducers (i.e., $f/1$, $f/2$, and $f/4$) and all window lengths are shown in Figs. 8, 9, and 10. In Fig. 8, the percent error in the scatterer size is compared to the known size for the three transducers for each of the different attenuation-

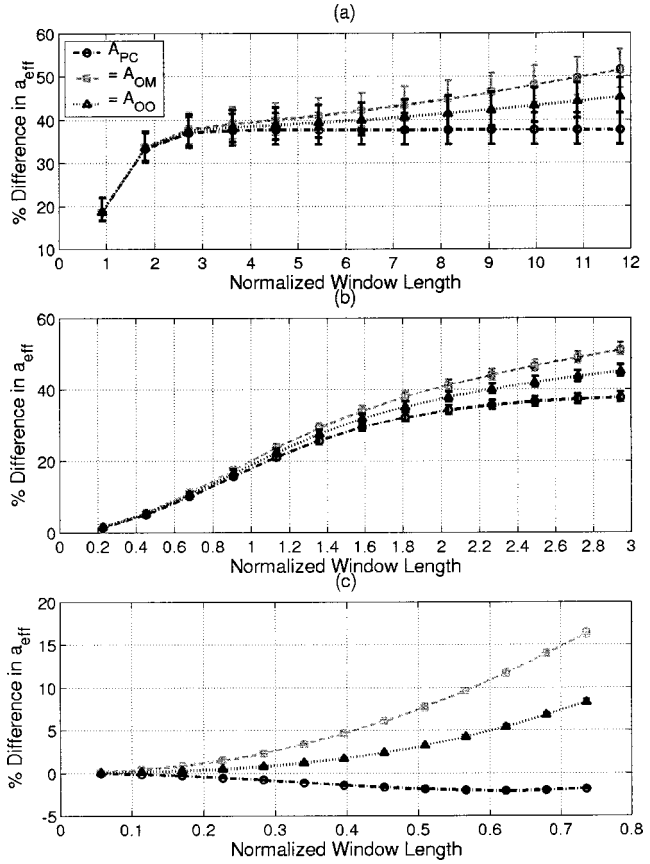

FIG. 10. The % difference between a_{eff} found using the traditional attenuation-compensation functions (A_{PC}, A_{OM}, and A_{OO}) when compared to a_{eff} found using A_{comp} in Eq. (26) versus window length normalized to the depth of focus (i.e., $7.08\lambda_o f\#^2$) at $\alpha = 0.5$ dB/cm/MHz for simulated fields from (a) $f/1$, (b) $f/2$, and (c) $f/4$ transducers.

compensation functions. The upper and lower error bars were found from

$$\sigma_{upper} = \frac{100}{a_{\text{eff}}|_{Theory}} \sqrt{\frac{\sum_{\forall a_{\text{eff}_j} > \overline{a}_{\text{eff}}} (a_{\text{eff}_j} - \overline{a}_{\text{eff}})^2}{\sum_{\forall a_{\text{eff}_j} > \overline{a}_{\text{eff}}} j}},$$
$$\sigma_{lower} = \frac{100}{a_{\text{eff}}|_{Theory}} \sqrt{\frac{\sum_{\forall a_{\text{eff}_j} < \overline{a}_{\text{eff}}} (a_{\text{eff}_j} - \overline{a}_{\text{eff}})^2}{\sum_{\forall a_{\text{eff}_j} < \overline{a}_{\text{eff}}}}}. \tag{37}$$

The accuracy of all estimates drops off significantly at smaller window lengths for all of the attenuation-compensation functions as a result of the convolution in the frequency domain associated with the windowing. In Fig. 9, the percent difference between the scatterer size given by the generalized attenuation-compensation function, A_{comp}, and the scatter size from the other attenuation-compensation functions are compared for the three transducers. It is clear that the error bars are reduced when the difference between the attenuation-compensation functions are found (Fig. 9) as compared to plotting the straight error values (Fig. 8). Hence, the differences between the different attenuation-compensation functions should be relatively constant between different scatterer distributions even though the absolute errors vary. Figure 10 shows the percent differences again but here the window length has been normalized with respect to the calculated depth of field for the transducer (i.e., $7.08\lambda_o f\#^2$)[20] where λ_o was the wavelength of the dominate frequency from the reference spectrum (i.e., V_{plane}).

The errors (Fig. 8) and differences (Fig. 9) in A_{OM}, A_{OO}, and A_{PC} are larger for the smaller *f*-number transducers (i.e., $f/1$ and $f/2$) and increase for longer window lengths. This makes sense because the importance of diffraction along the beam axis increases with increasing window length. Likewise, all four attenuation-compensation functions converge to the same result for decreasing window lengths. Oelze and O'Brien[18] also observed this when diffraction along the beam axis was neglected. Furthermore, A_{comp} yields excellent results regardless of window length or *f*-number and even provides improved estimates for the scatter size for long window lengths when the beam is relatively unfocused (i.e., $f/4$). Also, when the results for the $f/1$ and the $f/2$ transducers are compared, we see that the errors/differences plateau with increasing window length, so that the differences are greater for the $f/1$ transducer for smaller window lengths and then are approximately the same for large window lengths.

The plateau can be better illustrated by the results for the normalized window lengths (Fig. 10). The plateau is reached once the window length is several times the calculated depth of field (i.e., $7.08\lambda_o f\#^2$), hence, the contributing scatters are being limited by the focusing of the field and not by the windowing. Also, when comparing the differences between the $f/1$ and the $f/2$ transducers at the same normalized window length, the $f/2$ transducer has a larger difference for both the A_{OM} and A_{OO} estimates, and the A_{PC} estimate values converge to the same difference of 37.6% for normalized window lengths greater than approximately 2.5. Likewise, when comparing the differences between the $f/2$ and $f/4$ transducers at the same normalized window length, the $f/4$ transducer has a larger difference for the A_{OM} estimate. Also, for the $f/4$ transducer, the concavity of the A_{PC} estimate changed direction at a normalized window length of 0.65. Hence, A_{PC} may overestimate the scatterer size for large enough window lengths. Therefore, the error in using A_{OM} is greater for transducers with larger *f*-number when comparing across the same normalized window length, and the error in A_{PC} appears to plateau at sufficiently large normalized window length at approximately 37.6%. However, the performance of the attenuation-compensation functions cannot be generalized for small normalized window lengths for the different focused transducers.

The improvement in the estimates using the new generalized attenuation-compensation function can be illustrated further by considering the error in $\overline{a}_{\text{eff}}$ for different values of attenuation at set rectangular window lengths of 6 and 13 mm (Figs. 11 and 12, respectively). Notice that for the $f/1$ and $f/2$ transducers, A_{OM}, A_{OO}, and A_{PC} consistently overestimate the scatterer size on the order of 20% to 100% while A_{comp} gives almost exactly the right answer with errors typically less than 2%, with the largest error being 7.2%. However, for the $f/4$ transducer, although A_{OM} consistently overestimates the scatterer size, both A_{OO} and A_{PC} overestimate the scatterer size for small values of attenuation and then underestimate the scatterer size as the attenuation is in-

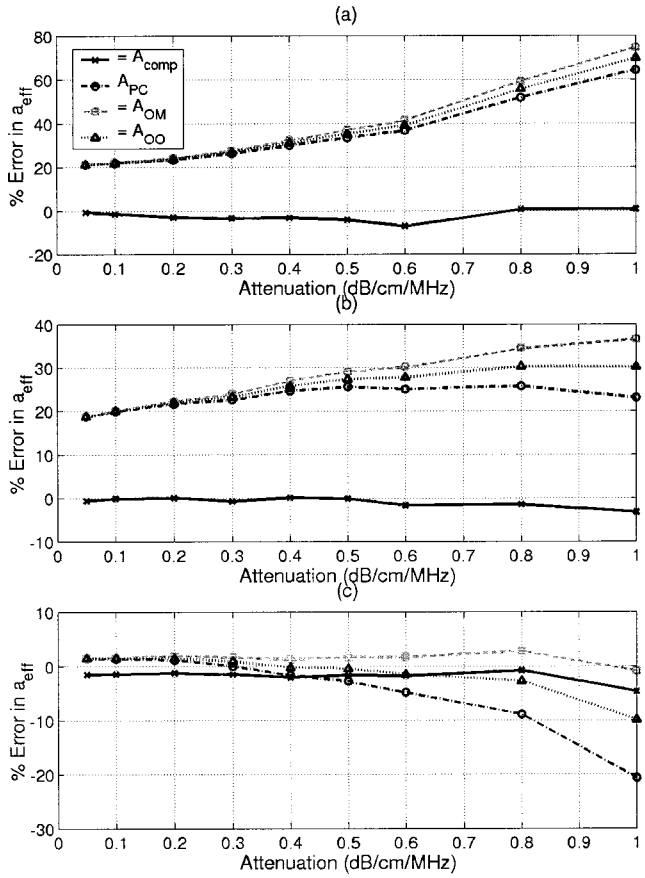

FIG. 11. The % error in $\overline{a}_{\text{eff}}$ when compared to known value of a_{eff} for $L=6$ mm for simulated fields from (a) $f/1$, (b) $f/2$, and (c) $f/4$ transducers for each of the attenuation-compensation functions (A_{comp}, A_{PC}, A_{OM}, and A_{OO}).

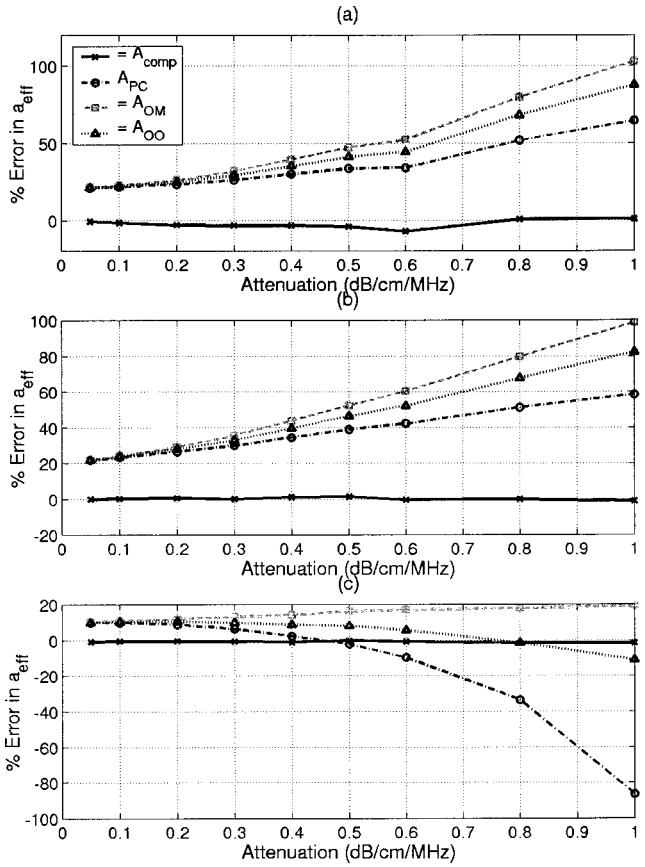

FIG. 12. The % error in $\overline{a}_{\text{eff}}$ compared to known value of a_{eff} for $L=13$ mm for simulated fields from (a) $f/1$, (b) $f/2$, and (c) $f/4$ transducers for each of the attenuation-compensation functions (A_{comp}, A_{PC}, A_{OM}, and A_{OO}).

creased. This is in agreement with Oelze and O'Brien[18] who also observed that A_{OM} should overestimate the scatterer size and both A_{OO} and A_{PC} should underestimate the scatterer size for long window lengths when diffraction along the beam axis can be neglected. The results for A_{PC} also agree with our predictions that A_{PC} will under/overestimate the scatterer size based on the relative importance of α and w_z. Once again, A_{comp} gives consistently good results for all attenuation values for the $f/4$ transducer with errors less than 5%. Hence, including diffraction along the beam axis with the generalized attenuation-compensation function improves the accuracy of the scatterer size estimate and allows for more strongly focused sources (i.e., $f/1$ and $f/2$) to be used in the data acquisition.

Although the accuracy of the scatterer size estimate is an important measure of the performance of the estimator, the precision of the estimate is also of great importance when performing tissue characterization. Figure 13 shows the deviations in the scatterer size calculated from Eq. (35) for each of the attenuation-compensation functions at a window length of 6 mm for all three of the transducers. Results at other window lengths are typically comparable to within a few percent. Notice that there is a slight degradation in the precision of the algorithms with increasing attenuation (i.e., change on the order of 8% from 0.05 to 1 dB/cm/MHz) and with decreasing *f*-number (i.e., change on the order of 8% from $f/1$ to $f/4$). These losses in precision may be a result of having fewer scatterers contributing to the backscattered signal as well as having the ka_{eff} values shift out of the optimal range[7] of $ka_{\text{eff}}=0.5\rightarrow1.2$ due to the increased attenuation (i.e., from $ka_{\text{eff}}=0.67\rightarrow1.6$ to $ka_{\text{eff}}=0.26\rightarrow0.96$). Also, although the precision of the different attenuation-compensation functions are comparable, A_{comp} is slightly less precise than the other algorithms for the $f/1$ and $f/2$ transducers (i.e., change on the order of 1% to 7%). This loss in precision, however, is insignificant compared to the simultaneous gain in accuracy.

V. DISCUSSION

In this paper, we considered the effects of focusing on estimating the size of scatterers in random media. Our development did not address estimating acoustic concentration although the derived equations would still be applicable. In our analysis, we assumed that the velocity potential field near the focus can be modeled as a three-dimensional Gaussian beam, the scatterers are a sufficient distance from the source, and the field is approximately constant across the scatterer. Our derivations demonstrated that correcting for focusing along the beam axis when obtaining estimates of scatterer size requires a generalized attenuation-compensation function that includes attenuation, windowing, and diffraction. Furthermore, our results provided insight into the applicability and

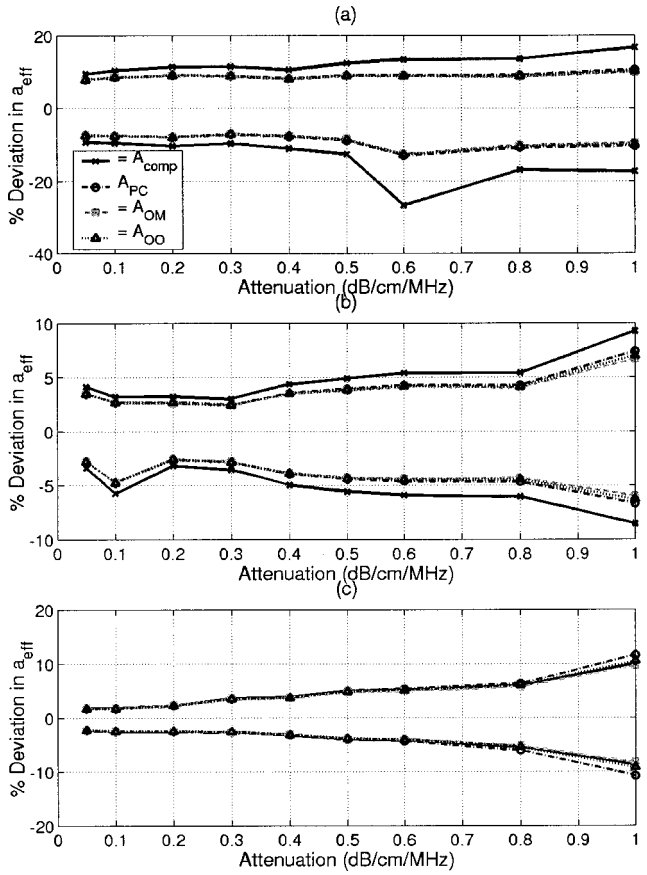

FIG. 13. The % deviations in the a_{eff} for a window length of 6 mm for each of the attenuation-compensation functions (A_{comp}, A_{PC}, A_{OM}, and A_{OO}) for simulated fields from (a) $f/1$, (b) $f/2$, and (c) $f/4$ transducers. The upper curves in each plot are the values of σ_{upper} and the lower curves in each plot are σ_{lower}.

robustness of previous attenuation-compensation functions in light of diffraction along the beam axis. Our theoretical work was also extended to diagnostically relevant fields where the transmit and receive foci are not necessarily at the same depths.

Also, an analysis of A_{comp} in Eq. (18) can also provide insight into the reference phantom methods proposed[13] that could also potentially correct for focusing. Using a reference phantom would be equivalent to applying Eq. (18) provided that the attenuation of the reference phantom was the same as the attenuation of the tissue. When the two values of attenuation are different, the value of the integrand [i.e., $g_{win}(s_z)\exp(-4(s_z^2/w_z^2))\exp(4\alpha s_z)$] would be different because the value of α would not be the same. The significance of this difference may be minor, but should be investigated before the reference phantom technique is generally accepted.

The Gaussian approximation of the velocity potential field in the focal region was also validated by comparing the approximation to complete calculated fields for a focused source. The approximation was found to be sufficiently accurate for all of the frequencies and degrees of focusing tested. In addition, the validity of the approximation was the same regardless of the degree of focusing (i.e., compare results for $f/1$ and $f/2$). Hence, our theoretical analysis should be valid for all of the sources encountered in clinical practice. However, the Gaussian approximation would be improved if the ultrasound system were engineered to reduce the side lobe structure observed for the ideal focused sources.

In our simulation analysis, we demonstrated that including the effects of diffraction along the beam axis improves the accuracy of the scatterer size estimator even for a weakly focused $f/4$ transducer when the pressure fields at the focus had a three-dimensional Gaussian distribution. The improvement in accuracy for the more strongly focused $f/1$ and $f/2$ transducers was on the order of 20% to 100% depending on the length of the window and the amount of attenuation without a significant loss in precision. Hence, using the generalized attenuation-compensation function allows for the use of focused sources when estimating scatterer properties that otherwise would not give usable results. Therefore, the new generalized attenuation-compensation function gives extensive improvement over the traditional methods.

ACKNOWLEDGMENTS

This work was supported by the University of Illinois Research Board, by a NDSEG Fellowship awarded to T. A. Bigelow, and by a Beckman Institute Graduate Fellowship awarded to T. A. Bigelow.

[1] R. C. Chivers and C. R. Hill, "A spectral approach to ultrasonic scattering from human tissue: methods, objectives, and backscattering measurements," Phys. Med. Biol. **20**(5), 799–815 (1975).
[2] J. C. Gore and S. Leeman, "Ultrasonic backscattering from human tissue: a realistic model," Phys. Med. Biol. **22**(2), 317–326 (1977).
[3] F. L. Lizzi, M. Greenebaum, E. J. Feleppa, and M. Elbaum, "Theoretical framework for spectrum analysis in ultrasonic tissue characterization," J. Acoust. Soc. Am. **73**, 1366–1373 (1983).
[4] M. F. Insana, R. F. Wagner, D. G. Brown, and T. J. Hall, "Describing small-scale structure in random media using pulse-echo ultrasound," J. Acoust. Soc. Am. **87**(1), 179–192 (1990).
[5] F. L. Lizzi, M. Astor, T. Liu, C. Deng, D. J. Coleman, and R. H. Silverman, "Ultrasonic spectrum analysis for tissue assays and therapy evaluation," Int. J. Imaging Syst. Technol. **8**, 3–10 (1997).
[6] M. L. Oelze, J. F. Zachary, and W. D. O'Brien, Jr., "Characterization of tissue microstructure using ultrasonic backscatter: theory and technique optimization using a Gaussian form factor," J. Acoust. Soc. Am. **112**, 1202–1211 (2002).
[7] M. F. Insana and T. J. Hall, "Parametric ultrasound imaging from backscatter coefficient measurements: image formation and interpretation," Ultrason. Imaging **12**, 245–267 (1990).
[8] E. L. Madsen, M. F. Insana, and J. A. Zagzebski, "Method of data reduction for accurate determination of acoustic backscatter coefficients," J. Acoust. Soc. Am. **76**(3), 913–923 (1984).
[9] M. F. Insana, E. L. Madsen, T. J. Hall, and J. A. Zagzebski, "Tests of the accuracy of a data reduction method for determination of acoustic backscatter coefficients," J. Acoust. Soc. Am. **79**, 1230–1236 (1986).
[10] K. A. Wear, M. R. Milunski, S. A. Wickline, J. E. Perez, B. E. Sobel, and J. G. Miller, "Differentiation between acutely ischemic myocardium and zones of completed infarction in dogs on the basis of frequency-dependent backscatter," J. Acoust. Soc. Am. **85**, 2634–2641 (1989).
[11] J. F. Chen, J. A. Zagzebski, and E. L. Madsen, "Tests of backscatter coefficient measurement using broadband pulses," IEEE Trans. Ultrason. Ferroelectr. Freq. Control **40**(5), 603–607 (1993).
[12] T. J. Hall, E. L. Madsen, J. A. Zagzebski, and E. J. Boote, "Accurate depth-independent determination of acoustic backscatter coefficients with focused transducers," J. Acoust. Soc. Am. **85**, 2410–2416 (1989).
[13] A. Gerig, J. Zagzebski, and T. Varghese, "Statistics of ultrasonic scatterer size estimation with a reference phantom," J. Acoust. Soc. Am. **113**, 3430–3437 (2003).
[14] P. M. Morse and K. U. Ingard, *Theoretical Acoustics* (McGraw–Hill, New York, 1968).

[15] P. Z. Peebles, *Probability, Random Variables, and Random Signal Principles*, 3rd ed. (McGraw–Hill, New York, 1993).
[16] K. A. Wear, ''A Gaussian framework for modeling effects of frequency-dependent attenuation, frequency-dependent scattering, and gating,'' IEEE Trans. Ultrason. Ferroelectr. Freq. Control **49**(11), 1572–1582 (2002).
[17] M. O'Donnell and J. G. Miller, ''Quantitative broadband ultrasonic backscatter: an approach to nondestructive evaluation in acoustically inhomogeneous materials,'' J. Appl. Phys. **52**(2), 1056–1064 (1981).
[18] M. L. Oelze and W. D. O'Brien, Jr., ''Frequency-dependent attenuation-compensation functions for ultrasonic signals backscattered from random media,'' J. Acoust. Soc. Am. **111**, 2308–2319 (2002).
[19] D. S. Ellis and W. D. O'Brien, Jr., ''The monopole-source solution for estimating tissue temperature increases for focused diagnostic ultrasound,'' IEEE Trans. Ultrason. Ferroelectr. Freq. Control **43**(1), 88–97 (1996).
[20] G. S. Kino, *Acoustic Waves: Devices, Imaging, and Analog Signal Processing* (Prentice–Hall, Englewood Cliffs, NJ, 1987).
[21] F. E. Barber, ''The scanning acoustic microprobe: I. Analysis and synthesis of a spherically symmetric point spread function,'' J. Acoust. Soc. Am. **90**, 1–10 (1991).